A Novel Method for Spectral and Spatial Characterisation of Flames Using a Custom-Developed Hyperspectral Imaging System

Yufeng Lai[a], Xuanqi Liu[b,c,*], Matthew Davies[a], Callum Fisk[a], Yunbai Wang[a], Songsong Meng[d], Hao Yang [b,c], Jiansheng Yang[e], Matthew Hobbs[a], Yang Zhang[f], Jon R. Willmott[a]

[a] *Department of Electronic and Electrical Engineering, The University of Sheffield, Sheffield, S1 4ET, United Kingdom*
[b] *School of Low-Carbon Energy and Power Engineering, China University of Mining and Technology, Xuzhou 221116, China*
[c] *Research Centre for Smart Energy, China University of Mining and Technology, Xuzhou 221116, China*
[d] *Department of Civil and Structural Engineering, The University of Sheffield, Sheffield, S1 3JD, United Kingdom*
[e] *The Electrical Engineering College, Guizhou University, Guiyang, China*
[f] *Department of Mechanical Engineering, The University of Sheffield, Sheffield S1 3JD, United Kingdom*

Abstract

This study introduces a pioneering approach to flame diagnostics by employing a radiometrically calibrated Hyperspectral Imaging (HSI) system to visualise the radiant power of methane-air flames both spectrally and spatially, a first in combustion research literature. Traditional flame diagnostic techniques rely heavily on chemiluminescence, with limitations in accurately depicting the physical radiative heat release and energy quantification. Our methodology involved the indirect calibration of a HSI system using a radiometer after comprehensive pre-calibrations and corrections for non-uniformities attributable to optical and electronic components, enhancing the accuracy and reliability of our radiant power measurements. The calibrated radiant power was validated against conventional chemiluminescence measurements with the comparisons of the peak C_2*(0,0)/CH* ratio. The calibrated HSI system enabled the detailed mapping of radiant power emitted by various radicals, notably different types of C_2*and CH*, within the hydrocarbon flames. Our results revealed distinct emission distributions and corresponding concentrations, highlighting the diverse roles of these radicals in the combustion process. We presented spatially resolved maps depicting the variations in radiant power and C_2*/CH* ratios, providing a direct visualisation of dominated energy-release radical distributions at different equivalence ratios. These visualisations serve as a promising tool for advancing our understanding of flame behaviours, combustion dynamics and energy conversion efficiency. The methodology developed in our work could offer valuable data for simulations and mechanism studies and contribute substantially to both academic research and practical applications in combustion technology.

Keywords: Radiant power; Hyperspectral imaging; Radiometer; Flame diagnostics; Visualisation

---

*Corresponding author.

1. Introduction

Flame diagnostics stand central to advancing our understanding of combustion processes, providing essential insights into the intricate dynamics and characteristics of flames that are critical for energy optimisation, pollution reduction, and safety enhancement [1] [2]. 2D flame imaging and chemiluminescence research have been widely used to interpret combustion behaviours, such as equivalence ratio measurement [3] [4], characterisations of oscillations [5], and chemical reactions [6] [7]. While these methods have been instrumental, traditional flame visualisation and chemiluminescence based on optical intensity have inherent limitations: they do not directly reflect the physical radiative heat release, and the intensity measurements could be biased due to optical and electronic factors. Moreover, the intensity or brightness does not typically reflect the actual energy involved, ignoring essential considerations such as bandwidth of the emitting radicals, demonstrating the need for actual radiant power measurements in combustion studies [8].

Conventionally, radiant power in flames has been measured using radiometers that capture the radiant power on a global scale, offering large fields of view but lacking spectral or spatial details [9] [10]. Although this approach can measure the total radiative heat release, it could miss the critical subtleties inherent in the combustion process.

The combustion process is consisting of complicated elementary reactions, producing various types of radicals for the progress of reactions. During this process, some radicals at excited state can be produced, resulting in the spontaneous luminescence when they decay to ground state. For a typical hydrocarbon flame, OH*, CH*, C_2* and CO_2*radicals are of particular significance, due to their close correlations with the combustion behaviours [6] [11]. In visible spectrum range, CH* and C_2* have significant luminescence intensity and strong correlations with key heat releasing reactions, making them become effective heat release markers and flame front indicator [12]. However, the spontaneous luminescence of a hydrocarbon flame in the VIS can be very complicated, due to the co-existence of C_2* swan band [13], CO_2* continuum [14] and other radicals related to NOx production[15]. Furthermore, premixed flames can be divided into specific regions, where are dominated by different chemical reactions [16]. This can result in the difference in luminescence intensity of radicals and the changes in the relative relationship between them. Therefore, obtaining the diagnostic data with both spectral and spatial resolution, which allows for precise identification of different radicals and their distributions, can be important for the combustion behaviours characterisations. Having an instrument that can conduct the flame reconstruction based on the emitted radiance with both spectral and spatial information is desired.

Hyperspectral imaging (HSI) emerges as a promising tool in this scenario, which can obtain both spectral and spatial information [17] [18]. HSI adds a third dimension of colour to a two-dimensional image, thus creating three-dimensional data cube[19]. One significant gap in the employment of HSI in combustion is the lack of energy calibration. Accurate radiant power readings combined with the advantages of HSI could provide invaluable insights in practical combustion applications with the visualisation of the energy map displaying the emission from individual radicals and their distributions.

Our objective was to develop an instrument which can allow use to visualise the radiant power with high spectral and spatial resolution. The methodology involved an indirect calibration with the radiometer after comprehensive pre-calibrations and corrections for each instrument. We aimed to produce a spectrally and spatially resolved radiant power map of hydrocarbon flames for the first time in the literature, offering a new dimension in combustion diagnostics enabling more precise analysis of flame characteristics and providing critical data for refining combustion modelling.

2. Methodologies

2.1 Experimental arrangement

The experimental setup consisted of three parts: premixed methane-air flame, radiometer, and HSI system, shown in Fig.1 (a). The nozzle of the burner has a 14.5 mm exit diameter and honeycombs as the flame stabiliser [20]. Methane and compressed air were premixed in a chamber with the set flowrates adjusted by the flow controller. The methane flow was set to 0.5 L/min while the air flow was set in the range from 2.0 L/min to 6.0 L/min to achieve the corresponding equivalence ratio range from 2.36 to 0.79.

The main objective in this study is to calibrate the HSI system for visualising the radiant power emitted from the flame spectrally and spatially. This was achieved with an indirect calibration using a radiometer. Radiometry is wildly used for measuring the heat release from the radiative heat transfer [21] [9] [10]. With comprehensive calibrations and optical corrections, the radiant power measured from the radiometer can be used as a calibration source for the same field-of-view (FOV) in the HSI. As illustrated in Fig.1 (a), the radiometer, which had a measured FOV of 2 mm, was precisely controlled by an adjustable height platform, and recorded the radiant power of the inner cone of the flame at an interval of height in 1 mm. The co-axis laser was used for alignment and focusing. Then the radiant power captured by the radiometer can be used for the calibration of the same FOV in

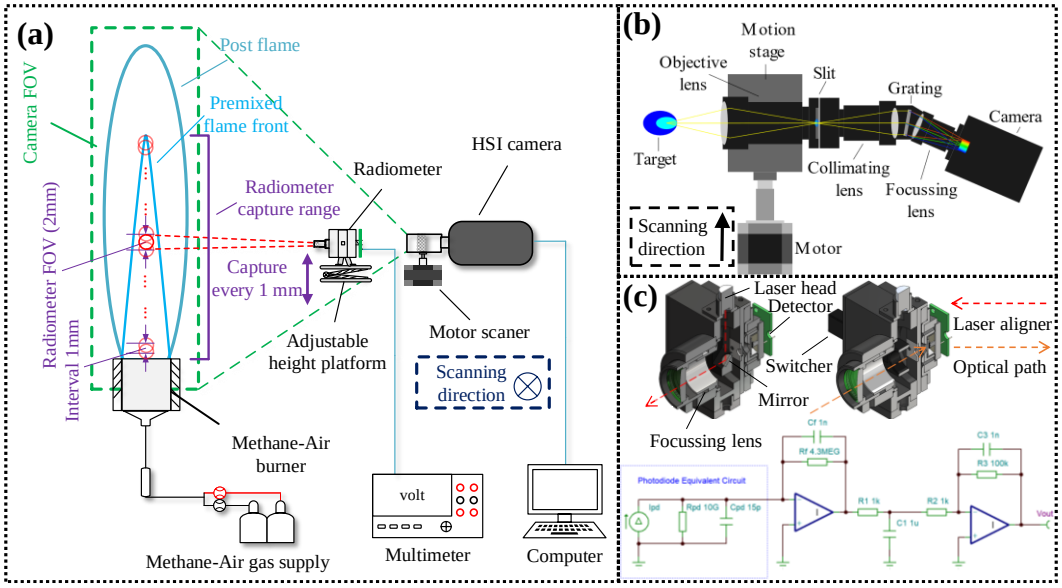

Fig. 1. Experimental arrangements. (a) Experimental setup. (b) HSI system. (c) Radiometer 3D model and circuit design.

the HSI. To eliminate the non-uniformity and bias in the optics and electronics, pre-calibrations were required for each instrument.

2.1.1 Hyperspectral imaging (HSI) system

To meet the specific requirements for flame diagnostics and ensure greater customisability, we custom-designed our own HSI system, shown in Fig. 1(b), which is based on the line-scanning hyperspectral principle [22][23][24]. The system comprised of three lens assemblies, a slit (75μm), a diffraction grating and a focal plane array (FPA) camera. The objective lens formed an image onto the vertical slit, which subsampled the image as a vertical slice. This slice was then collimated by a collimating lens before it passed through the transmission grating. The dispersed light was then refocussed onto the focal plane array of the camera, aligning each pixel row with the spectral intensity at specific positions along the slice. The objective lens was translated orthogonally to the slit and optical axis, allowing the slit to fully sample the target. The captured sequence of images was then restructured into a three-dimensional data array, with each image representing a different wavelength. The size each pixel (width and height respectively) occupied was measured preliminarily with scanning a 20 mm diameter aperture in the front of the furnace at the defined working distance and scanning speed.

2.1.2 Radiometer

The design of the radiometer is shown in Fig.1 (c). The radiometer consisted of a focussing lens, 500 nm long pass and 650 nm short pass filter combination, silicon photodiode, and a two-stage photodiode amplifier circuit. A

visible laser on the same optical path as the radiometer was used to align the radiometer with the flame before measurements were taken. A mirror was placed into the optical path of the radiometer during alignment so that the laser was on the same optical path and distance. A switcher was designed to control the mirror, allowing the switchover of alignment and measurement.

The equivalent circuit diagram for the photodiode and amplifier circuit is shown in Fig. 1 (c). The transimpedance amplifier stage had a cut-off frequency of 37 Hz, followed by a 159 Hz low pass filter to minimise the effects of high frequency electronic noise. A low cut-off frequency was chosen to ensure minimal measurement noise. An inverting amplifier stage was then used to increase the output signal further, reducing measurement uncertainty. The photodiode was operated in photovoltaic mode to minimise the effects of detector dark current. The effective gain of the circuit can be calculated as Eq. 1:

$$G = G_1 \cdot G_2 = -R_f \cdot -\frac{R_3}{R_2}, \quad (1)$$

where G (V/A) is the effective gain of the system, G_1 and G_2 are the transimpedance gain (V/A) and the second stage gain (V/V) respectively, R is the corresponding resistance. Therefore, the actual voltage generated can be calculated as Eq. 2:

$$V_{out} = I_{pd} \cdot G, \quad (2)$$

where V_{out} is the voltage measured from the radiometer (V) after the offset subtraction, I_{pd} is the photocurrent (A).

2.2 Calibrations

2.2.1 HSI calibrations

The calibration of the HSI system contained three aspects: spectral wavelength, spectral sensitivity and size-of-source effect (SSE), shown in Fig.2. The HSI was calibrated for wavelength range by targeting a Mercury-Argon lamp which produced a series of narrowband spectral lines of known wavelength. These lines could be identified

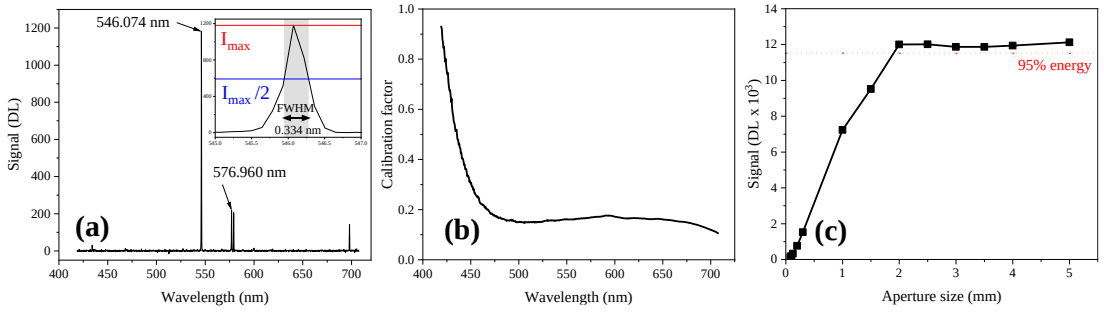

Fig. 2. HSI calibrations. (a) Spectral calibration using a Mercury Argon lamp. The resolution was determined by the FWHM. (b) Calibration factor obtained by the normalised ratio between Planck's curve and the camera captured. (c) SSE of the system.

in the raw output of the HSI by comparing their spacing and intensity to the NIST Atomic Spectra Database. The wavelength range covered 418 to 708 nm (Fig.2(a)). The spectral resolution of the system was determined by calculating the full width at half maximum (FWHM) of the spectral lines and was found to be 0.334 nm.

The HSI system can have non-uniform sensitivity across the spectral range, which is attributed to the factors including the responsivity of the camera sensor, the spectral efficiency of the diffraction grating and the intrinsic properties of light. The spectral sensitivity of the system had to be measured in order to ensure the relative spectral intensity that was measured would not be influenced by the system bias [25]. The temperature of a blackbody furnace (Land Instruments R1500T) was measured using a calibrated radiation thermometer (Land Instruments Cyclops C100L) and the corresponding spectral output was calculated using Planck's Law [26][27]. A calibration factor could then be obtained by taking a ratio of Planck's Law and the measured spectrum. The normalised calibration factor is shown in Fig. 2 (b). Spectra can be scaled according to the calibration factor and the true, relative spectral intensity could be determined. The camera used in this study has a well-assessed flat-field tolerance, as verified by the manufacturer. Additionally, the edge of the frame has been cropped to further enhance flatness as well as the offset variations have been removed with the dark correction. Therefore, the non-uniformity across the FPA is negligible.

SSE, as a critical concept in radiometry, is used to determine the minimum FOV or size of the radiance emitting objective that not significantly influences the signal received by the detector/camera sensor (95% of the maximum energy) [28]. The SSE measurement of the HSI can help the determining of the suitable FOV of the radiometer, ensuring the limited effects of lens aberrations and the scattered/stray optical radiation on the camera side. Different size apertures were placed in the front of the blackbody furnace and the averaged readings from the camera with varied apertures can be obtained, shown in Fig. 2 (c). The aperture size where 95% energy was received is around 1.8 mm which we defined as determining the minimum FOV of the radiometer.

2.2.2 Radiometer calibrations

The radiometer calibration involved three aspects: the optical efficiency of the system; the effective FOV of the radiometer at the defined working distance; and the noise analysis, shown in Fig.3.

Fig. 3 (a) shows the detector responsivity from the manufacturer datasheet and the optical transmission efficiency across the interested spectral range employing the 500 nm long pass and 650 nm short pass filers, which was precisely measured, within our laboratory, using a spectrometer (Thorlabs CCS200).

The FOV for our radiometer was carefully selected to balance the need to minimise flame region inhomogeneities while avoiding sensor bias. Consequently, the FOV was determined to be as small as possible

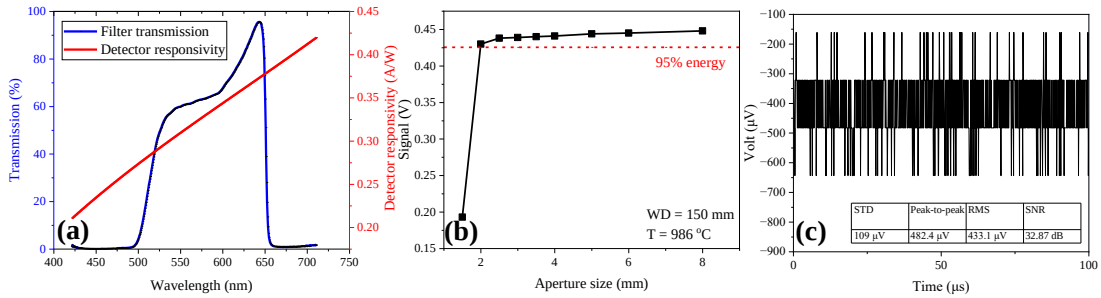

Fig. 3. Radiometer calibrations. (a) filter transmission and the detector sensitivity. (b) FOV of the radiometer, the aperture size in 95% energy received indicating the actual FOV (c) noise analysis.

while remaining larger than 1.8 mm (Fig.2 (c)) to minimise size-of-source effect. The FOV of the radiometer was measured using the same method described in 2.2.1 for the HSI system. The optics of the radiometer were adjusted until an effective FOV of 2 mm was achieved, with the measurement results shown in Fig. 3(b).

The noise performance was measured using a high-speed oscilloscope (Keysight MSOX3014T, 5GS/s) over a period of 100 μs, shown in Fig. 3 (c). The calculated signal-to-noise ratio (SNR) of 32.87 dB demonstrates that our circuit has less than 2.5% uncertainty. This measurement was considered a worst-case scenario because the resolution of the oscilloscope limited results to multiples of 39 μV.

2.2.3 Radiant power calibration

The HSI system was calibrated to retrieve true radiant power, using the calibration procedure described in Fig. 4. A measurement of the flame was made by targeting the reaction zone of the flame where the SNR was greatest with the radiometer and recording the voltage. The exact position of the radiometer's FOV in the flame could be determined with the alignment laser, shown in Fig.1 (c).

The generated photocurrent is proportional to the incident power on the detector, the detector responsivity, and transmission efficiency of the system at the desired wavelengths, presented in Eq. 3:

$$I_{pd} = \int_{\lambda_1}^{\lambda_2} \Phi(\lambda) \cdot R(\lambda) \cdot T(\lambda)\, d\lambda, \tag{3}$$

where λ_1, λ_2 represent the wavelength range of the system (418 nm and 708 nm), $\Phi(\lambda)$ is the radiant power, $R(\lambda)$ is the spectral responsivity of the radiometer detector (A/W) and $T(\lambda)$ is the spectral transmission of optical filters (norm.).

Thus, the voltage measured by the radiometer can be determined by rearranging Eq. 2 and 3:

$$V_{out} = G_1 \cdot G_2 \cdot \int_{\lambda_1}^{\lambda_2} \Phi(\lambda) \cdot R(\lambda) \cdot T(\lambda)\, d\lambda. \tag{4}$$

The uncalibrated signal from the HSI system can be related to optical power by Eq. 5:

$$S_{HSI}(\lambda) = \frac{1}{k \cdot K(\lambda)} \cdot \Phi(\lambda), \tag{5}$$

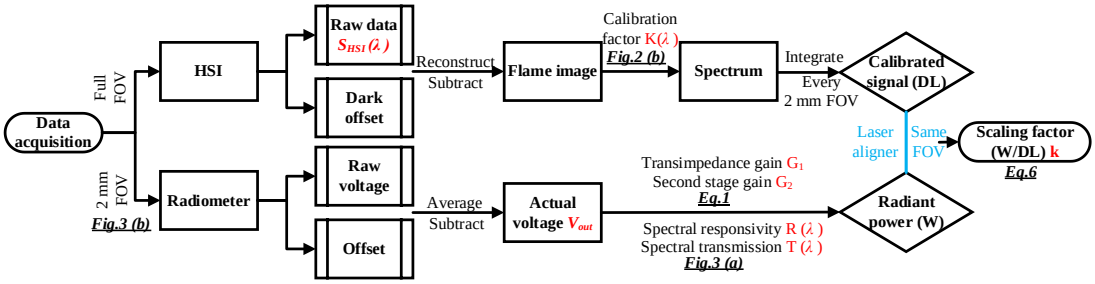

Fig. 4. Radiant power calibration procedures.

where k is a scaling factor (W/DL), $S_{HSI}(\lambda)$ is the uncalibrated signal from HSI system (DL), $K(\lambda)$ is the calibration factor of the system described in section 2.2.1 (arb.)

By summing the signal in the HSI corresponding to the FOV of the radiometer, the scaling factor k can then be determined by combining Eq.4 and 5 to Eq. 6:

$$k = \frac{V_{out}}{G_1 \cdot G_2 \cdot \int_{\lambda_1}^{\lambda_2} S_{HSI}(\lambda) \cdot K(\lambda) \cdot R(\lambda) \cdot T(\lambda) d\lambda}, \quad (6)$$

The units of k are W/DL and so this value can be used to convert from the calibrated HSI signal in DL to W by rearranging Eq. 5:

$$\Phi(\lambda) = k \cdot S_{HSI}(\lambda) \cdot K(\lambda) \quad (7)$$

2.3 Data analysis

The flame images can be obtained by reconfiguring the spatial-spectral dimensions of the raw data cube. The images were segmented based on a global threshold determined by identifying the inflection point where a noticeable change in the gradient of the intensity profile was observed. The results of the segmentation are shown in Fig. 5. This algorithm performed well in segmenting the whole flame profile, including the outer cone (post-flame region) and the inner cone, which is the projection of flame reaction front in the 2D image. The active flame zones can be isolated, ensuring a consistent basis for comparison across different experimental conditions.

We conducted a spectral analysis on segmented flame regions, integrating observed data across specific wavelength intervals to examine the radiant energy emitted by C_2*, CH* radicals and water vapour within their

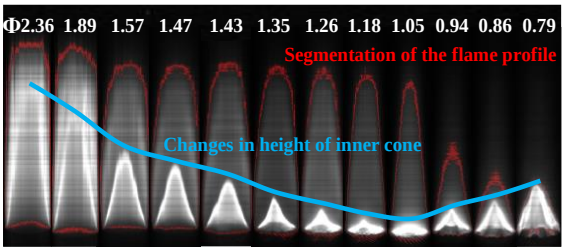

Fig. 5. Flame segmentation results with different Φ.

corresponding spectral bands. The wavelengths of each band of interest were identified using the HITRAN database [29]. This method facilitated a detailed examination of the variations in radiant power emitted by different radicals, further allowing the calculation of the ratios of individual C_2* against CH* by comparing the integrated energy values. The total radiant power, integrated within the segmented flame, was used to provide quantitative results against varied equivalence ratios.

Building on the integrated spectral data, we generated colour maps that visually represent the distribution of radiant power within the segmented flame regions. These maps, created for both individual radiant power and their corresponding ratios, provide insights into the spatial heterogeneity of chemical reactions occurring within the flame.

For the first time in literature, we present visual mappings of the radiant power emitted by individual radicals and molecules, as well as the ratios of various C_2* radicals to CH*, enabling a new approach for visualising the combustion process in terms of energy. By comparing these maps across different equivalence ratios, we can directly observe and analyse changes in the chemical dynamics of the combustion process, contributing to a deeper understanding of the factors influencing flame behaviour and energy conversion efficiency. Furthermore, the high-fidelity images could provide insights when registered with simulations.

The adaptability of the developed HSI system allows it to be extended to various combustion environments, making it a valuable tool for broader flame diagnostics. While this study focused on hydrocarbon flames, the same methodology can be applied to other fuel types by tailoring the optical components, such as the diffraction grating and FPA, to match the emission characteristics of different combustion radicals. This capability enhances the system's potential for investigating alternative fuels, including hydrogen, syngas, and ammonia, which have distinct spectral emissions.

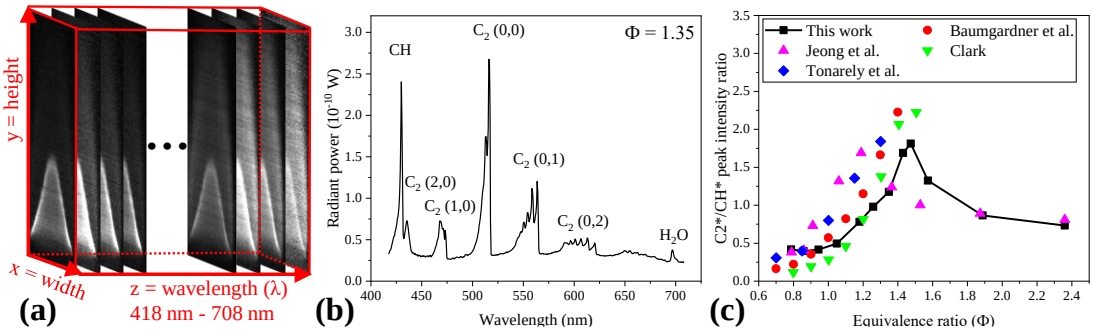

Fig. 6. (a) Reconstructed HSI data cube (b) Methane-air flame spectrum (Φ = 1.35) based on the calibrated radiant power (c) C_2*(0,0)/CH* peak intensity ratios against equivalence ratio, compared with other work.

3. Results and discussions

3.1 Data acquisition

The HSI flame data cube can be obtained following the procedures illustrated in Fig.4. The example output images are shown in Fig. 6 (a). The reconstructed hyperspectral images show a good spatial resolution presenting the clear edge of the flame and the layer of the reaction front. Fig. 6(b) shows the spectrum of the methane-air flame at $\Phi = 1.35$, obtained by integrating the calculated radiant power along the segmented flame profile. Addition to the high spectral resolution (0.334 nm, shown in Fig.2 (a)) of the present system, the different radicals in the Swan band can be identified spectrally and spatially. The radicals and species of interest are shown in Fig.6 (b) based on HITRAN database [29].

While the traditional chemiluminescence (used intensity spectrum) [1] [3] provides valuable insights into the emission characteristics of various species, the energy-based spectrum, as obtained in our study, delves deeper into the energetics of the combustion process. Although the general shape of the spectra in energy and intensity representations should be similar due to corresponding quantum mechanical transitions and the inherent nature of radiative emissions, they convey fundamentally different aspects of the behaviours of flame. The intensity spectrum, often considered as a measure of 'brightness' or 'visibility,' represents an uncalibrated intensity that lacks physical insights into radiative heat release. In contrast, the energy-based spectrum accounts for the actual photonic energy being emitted, representing critical information about the thermal and chemical states of the reacting species in combustion process.

Fig. 6 (c) illustrates the comparisons between the conventional chemiluminescence measurements [30][31][32][33], specifically focusing on the C_2* (0,0)/CH* peaks ratio, and the peaks ratio obtained from the presented work. The results agreed well with the previous work, which indicates the validity of the spectral

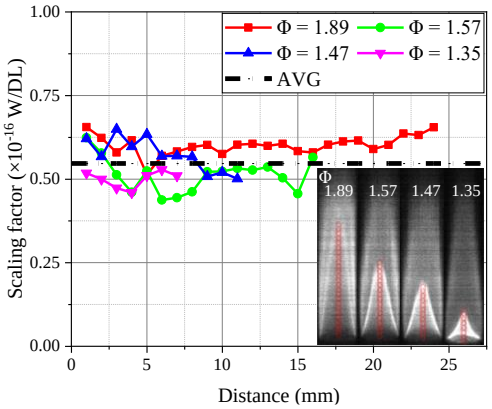

Fig.7 The calculated scaling factors. Flame images show the alignment with radiometer FOVs (red ellipses).

calibration methods employed in this work. The similarity in trend patterns between the intensity and energy ratios suggests that the same physical phenomena were being observed, but with different interpretive approaches. It is worth noting that the peak ratios of the radiant energy were employed when compared with the previous work for consistency. However, the energetic insights obtained in the integrated values across each radical spectral band, which carry more substantial physical implications, will be the focus in the subsequent sections.

3.2 Calibration results

A critical step for the radiant power calibration was based on the precision of the scaling factor (k) calibration. A key aspect of ensuring the accuracy is the alignment of the FOV of the radiometer with the same spatial segment of the hyperspectral image. With the help of the co-axial laser indicator, and the comprehensive measurements of the optical performance which were demonstrated in Section 2, the FOV of the two instruments were aligned for the calibration, shown as the flame images in Fig.7. Each red ellipse represents a FOV of the radiometer and the practical partial segmentation in the HSI flame.

Theoretically, the scaling factor should remain consistent, regardless of the changes in location, and equivalence ratio, because the pre-calibrations have eliminated the variables and inconsistency caused by the spectrum. To ensure repeatability, measurements were performed for four different equivalence ratio flames, focusing on the inner flame, due to the better stability and SNR observed in these regions.

The scaling factors were calculated based on Eq. 6, as shown in Fig.7.The consistency of these calculated scaling factors, across different conditions, indicates the reliability of our calibration methodology. The results were averaged across all conditions to reduce the inconsistency caused by operator error, shown as the black dotted line in Fig. 7.

3.3 Radiant power mapping

Following the procedures described in Fig.4, the radiant power can be mapped spatially and spectrally, as shown in Fig. 8(a) and (b). The radiant power mapping provides the ability to visualise the distribution of the energy emitted by each radical.

The radiant power maps of integrated C_2* radicals (C_2* all) under varying equivalence ratios (Φ) are shown in Fig. 8(a) as examples to illustrate the change in emitting energy with different Φ. It is found that the radiance emitted by C_2* radicals significantly change both in its intensity value and the distributions. From Φ 2.36 to 1.05,

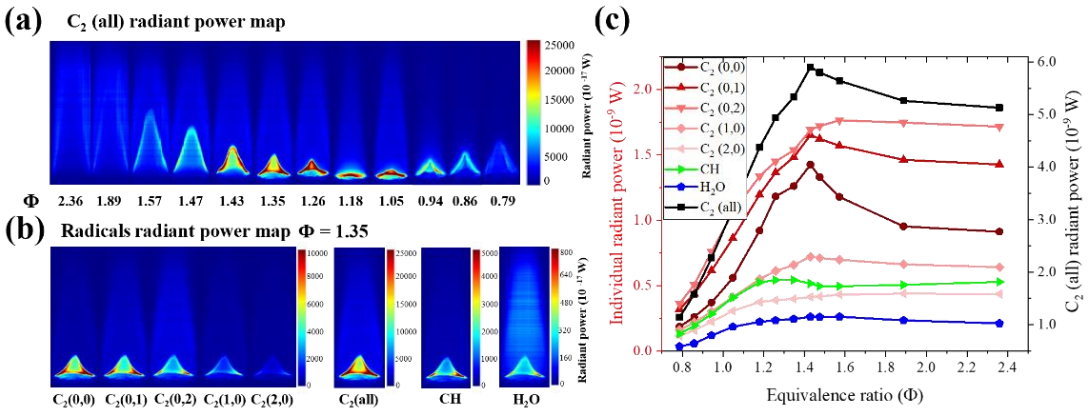

Fig. 8. The radiant power maps of the radiating radicals. (a) C_2* (all) radiant power map at different Φ. (b) Radiant power map of different radicals at Φ = 1.35. (c) The radiant power of the different radicals integrated along segmented flame

the inner cone exhibits an increase in intensity, coupled with a decrease in size. This phenomenon can be attributed to the higher concentration of reactive species, local temperature and heat release in the region, leading to more intense radiation of all the C_2* radiative radicals [6][12]. The inner flame expands as the Φ shifts from 1.05 to 0.79, indicating the radiant power intensity diminishes. This could be attributed to the leaner mixture and lower temperature at these lower Φ, which tends to produce less intense radiation. The change in the reaction zone position and size indicate the flame speed and the flow rate balance shift [34].

Apart from the radiant power change with different Φ, the radiant power emitted by different radicals can vary significantly when under the same flame conditions [35]. Fig. 8(b) illustrates the differences in radiant power distribution among various radicals, and H_2O vapour at Φ = 1.35. It can be observed that the radiant power emitted by each radical is not only different in the global intensity but also in its spatial distributions. For instance, C_2*(0,0) radiation was predominantly concentrated in the inner flame, with minimal presence in the outer regions. This localisation reflected the high-energy reactions typically confined to the inner cone, where both C_2* and CH* radical concentrations were dense. Conversely, C_2* (0,2) displays substantial radiant energy in the outer flame, suggesting that there was considerable concentration of C_2* (0,2) radicals distributed in the outer flame. This could suggest that C_2* (0,2) plays a crucial role in the secondary combustion reactions occurring in the post flame region. H_2O vapour employed a more complex absorption-emission process; its emission map displayed a considerable radiant emission in the outer flame, consistent with the completion of combustion reactions and the presence of product species in this cooler, post-combustion region.

Fig. 8(c) presents the quantitative results, integrating data across the segmented flame profile. Overall, the radiant power increased with higher Φ until it dropped again after Φ = 1.45. This agrees with existing data in the trends of C_2* and CH* intensity [32] [31]. The peak radiant power point in Fig 8 (c) indicates where the highest

efficiency energy conversion occurs and its corresponding Φ. The various C_2* radicals exhibited slightly different trends. These discrepancies in radiant power curves presented the unique transition probabilities involved in the formation of different C_2* species [36]. Such differences are crucial for understanding the energy dynamics during combustion.

3.4 Radiance power ratios distributions

The ratio between C_2* and CH* is crucial in conventional chemiluminescence because the ratio may act as an indicator of Φ [17]. Analysing the radiant power ratios of different radicals in the present work provided new insights into the reaction dynamics for several reasons: 1. The radiant power ratios directly represent the energy conversion/release by each radical. 2. The higher spectral resolution highlights the individual C_2* radicals in relation to CH*. 3. Mapping ratio distributions reveals local reaction characteristics, offering insights into spatial variability of reactions within the flame.

Fig. 9(a) shows the C_2* (all)/CH* radiant power ratio maps at various Φ. Along the Φ (0.79 – 2.36), it is observed that the C_2*/CH* ratio in the reaction zone was lower than in the post region. This phenomenon indicates a more significant presence of CH* radicals in the inner cone, due to more rapid formation in the reaction region, resulting in a relatively lower C_2* concentration than CH*. The distribution highlights the key role of CH* in energy conversion within the inner cone, while C_2* significantly contributes to radiative emissions during secondary combustion, primarily occurring in the post-flame region.

When the flame becomes richer in fuel (Φ 1.05 - 2.36) the C_2*/CH* ratio in the whole flame region, particularly in the inner cone, increased with a rising Φ, suggesting enhanced C_2* formation ratio with richer mixtures. This is

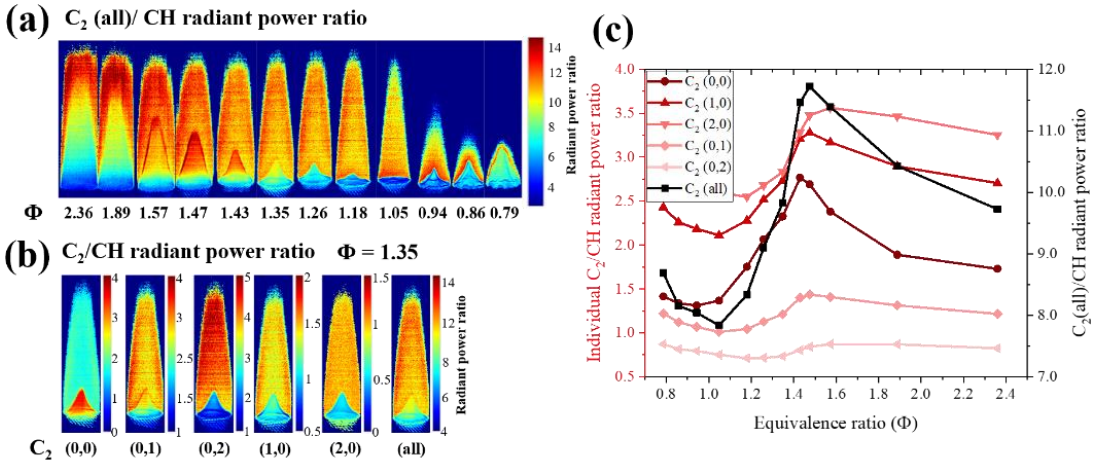

Fig. 9. The radiant power ratios of C_2*/CH*. (a) C_2* (all)/CH* radiant power ratio map at different Φ. (b) Radiant power ratio map of different C_2* radicals against CH* at Φ = 1.35. (c) The radiant power ratios of varied C_2* /CH* of the flame.

possibly because oxygen is absent during the formation reactions of C_2*; insufficient oxygen leads to greater C_2* formation [6]. Interestingly, there was a higher C_2*/CH* ratio observed in the reaction zone than the post region at specific Φ (1.43 – 1.57). The interface was where the primary and secondary reactions met, leading to a transitional zone of combustion characteristics.

The radiant power ratios of individual C_2* radicals against CH* at Φ = 1.35 are shown in Fig. 9(b). The ratio corresponding to each C_2* radical exhibits a distinct pattern, indicating the diverse roles and reaction pathways involved. For C_2* (0,0), the ratio is higher in the inner cone than the post region, showing a significant concentration of this radical generated in the reaction zone. C_2* (0,1) presents a more uniform distribution between the zones, suggesting its involvement across a broader reaction front. In contrast, C_2*(0,2), C_2*(1,0), and C_2*(2,0) are prominently higher in the post-flame, indicating their critical roles in the secondary combustion.

Fig. 9(c) shows the quantitative results integrated along the flame profiles. The trends were similar to the C_2*/CH* peak intensity of conventional chemiluminescent measurements [3] but in a different scale. It is found that the ratio relating to each C_2* radical presented varying trends against Φ, indicating that shifts in combustion chemistry disproportionately impact individual radicals and reflect their distinct roles and reactivities in the flame dynamics [35].

These radiant power ratios, especially the discrepancies observed for different C_2* radicals, emphasise the intricate and varied transitions in flame chemistry. The distinct spatial distributions and response to changing Φ reinforce the importance of these radicals in energy conversion processes.

4. Conclusions

In this study we have developed an innovative approach to visualise the radiant power emitted by methane-air flames spectrally and spatially for the first time in the literature. This was achieved by an indirect calibration of a hyperspectral imaging (HSI) system using a radiometer. Comprehensive pre-calibrations and corrections have been employed for both HSI and radiometer measurements to eliminate the non-uniformity and bias caused by the optics and electronics. The spectrum based on the calibrated radiant power was compared with conventional chemiluminescence for validation. The calibrated HSI system allowed us to map the radiant power emitted by various radicals and molecules, revealing distinctive emission distributions and their corresponding concentrations in the flame. The radiant power and the C_2*/CH* ratio maps presented in this work showed significantly different spatial distributions with various C_2* radicals. Additionally, their total radiant intensity also shows an obviously different against equivalence ratios.

Our pioneering approach marks an advancement in fundamental flame research, introducing a direct visualisation of the radiative emission which could serve as a promising instrument for in-depth explorations into energy efficiency and sustainability in combustion technologies and could provide valuable data for simulations and mechanism studies.

Author contributions

Y. Lai: Writing – review & editing, Writing – original draft, Visualisation, Validation, Software, Methodology, Investigation, Formal analysis, Data curation, Conceptualisation. **X. Liu:** Writing – review & editing, Validation, Methodology, Investigation, Data curation, Conceptualisation. **M. Davies:** Writing – review & editing, Methodology, Investigation, Software, Conceptualisation. **C. Fisk:** Writing – review & editing, Methodology, Investigation, Software. **Y. Wang:** Writing – review & editing, Methodology, Visualisation, Software. **S. Meng:** Writing – review & editing, Visualisation, Software. **H. Yang:** Writing – review & editing, Methodology, Investigation. **J. Yang:** Writing – review & editing, Methodology, Investigation. **M. Hobbs:** Writing – review & editing, Methodology, Conceptualisation. **Y. Zhang:** Writing – review & editing, Supervision, Resources. **J. R. Willmott:** Writing – review & editing, Supervision, Software, Resources, Project administration, Investigation, Conceptualisation.

References

[1] J. Ballester and T. García-Armingol, "Diagnostic techniques for the monitoring and control of practical flames," 2010, *Elsevier Ltd*. doi: 10.1016/j.pecs.2009.11.005.

[2] Y. Lai *et al.*, "Combustion inhibition of biomass charcoal using slaked lime and dolime slurries," *Fire Saf J*, p. 103841, Jun. 2023, doi: 10.1016/j.firesaf.2023.103841.

[3] J. Yang, Z. Ma, and Y. Zhang, "Improved colour-modelled CH* and C2* measurement using a digital colour camera," *Measurement (Lond)*, vol. 141, pp. 235–240, Jul. 2019, doi: 10.1016/j.measurement.2019.04.016.

[4] L. Zheng, T. Yang, W. Liu, Y. Lai, and J. Yang, "Enhancing Accuracy of Flame Equivalence Ratio Measurements: An Attention-Based Convolutional Neural Network Approach for Overcoming Limitations in Traditional Color Modeling," *Sensors*, vol. 24, no. 21, p. 6853, Oct. 2024, doi: 10.3390/s24216853.

[5] X. Liu, H. Zhou, Y. Lai, and Y. Zhang, "Characterisations of self-excited nonlinear oscillations at varied system parameters in a Rijke tube with a premixed laminar flame," *Exp Therm Fluid Sci*, vol. 146, Aug. 2023, doi: 10.1016/j.expthermflusci.2023.110923.

[6] J. Kojima, Y. Ikeda, and T. Nakajima, "Basic aspects of OH(A), CH(A), and C2(d) chemiluminescence in the reaction zone of laminar methane-air premixed flames," *Combust Flame*, vol. 140, no. 1–2, pp. 34–45, Jan. 2005, doi: 10.1016/j.combustflame.2004.10.002.

[7] M. Pan, X. Liu, Y. Lai, Y. Zhang, and Y. Zhang, "Resolving Visible Emission Lines in Hydrogen Diffusion Flames," 2024, doi: 10.3390/aerospace11120983.

[8] H. C. Zhou *et al.*, "Experimental investigations on visualization of three-dimensional temperature distributions in a large-scale pulverized-coal-fired boiler furnace," *Proceedings of the Combustion Institute*, vol. 30, no. 1, pp. 1699–1706, 2005, doi: 10.1016/j.proci.2004.08.090.

[9] M. Muñoz, J. Arnaldos, J. Casal, and E. Planas, “Analysis of the geometric and radiative characteristics of hydrocarbon pool fires,” *Combust Flame*, vol. 139, no. 3, pp. 263–277, Nov. 2004, doi: 10.1016/j.combustflame.2004.09.001.
[10] L. Karapateas, Y. Lai, X. Meng, Y. Zhang, J. R. Willmott, and M. J. Hobbs, “Si APD-Based High Speed Infrared Radiation Thermometry for Analysing the Temperature Instability of a Combustion Chamber,” 2024, doi: 10.3390/s24237780.
[11] H. Yang, Y. Lai, X. Liu, H. Jiang, and J. Yang, “Equivalence Ratio Modelling of Premixed Propane Flame by Multiple Linear Regression Using Flame Color and Spatial Characteristics,” *Measurement Science Review*, vol. 23, no. 1, pp. 40–46, Feb. 2023, doi: 10.2478/msr-2023-0005.
[12] J. Kojima, Y. Ikeda, and T. Nakajima, “Spatially resolved measurement of OH*,CH*, and C*2 chemiluminescence in the reaction zone of laminar methane/air premixed flames,” *Proceedings of the Combustion Institute*, vol. 28, pp. 1757–1764, 2000.
[13] S. Mashruk, X. Zhu, W. L. Roberts, T. F. Guiberti, and A. Valera-Medina, “Chemiluminescent footprint of premixed ammonia-methane-air swirling flames,” *Proceedings of the Combustion Institute*, vol. 39, no. 1, pp. 1415–1423, Jan. 2023, doi: 10.1016/j.proci.2022.08.073.
[14] J.-M. SAMANIEGO, F. N. EGOLFOPOULOS, and C. T. BOWMAN, “CO2* Chemiluminescence in Premixed Flames,” *Combustion Science and Technology*, vol. 109, no. 1–6, pp. 183–203, Nov. 1995, doi: 10.1080/00102209508951901.
[15] T. García-Armingol and J. Ballester, “Flame chemiluminescence in premixed combustion of hydrogen-enriched fuels,” *Int J Hydrogen Energy*, vol. 39, no. 21, pp. 11299–11307, Jul. 2014, doi: 10.1016/j.ijhydene.2014.05.109.
[16] S. H. CHUNG and C. K. LAW, “Burke–Schumann Flame with Streamwise and Preferential Diffusion,” *Combustion Science and Technology*, vol. 37, no. 1–2, pp. 21–46, May 1984, doi: 10.1080/00102208408923744.
[17] H. Yang *et al.*, “Experimental and Simulated Study of the Relationship between Color Camera Imaging and Color-Modeled Equivalence Ratio Measurement,” *IEEE Trans Instrum Meas*, vol. 72, 2023, doi: 10.1109/TIM.2023.3267359.
[18] B. Wang *et al.*, “Development of Equivalence Ratio Measurement Model of Premixed Methane Flames Using Hyperspectral Imaging of C2* and CH* Chemiluminescence and Random Forest Algorithm,” *Combustion Science and Technology*, 2024, doi: 10.1080/00102202.2024.2306899.
[19] Z. You *et al.*, “Machine Learning-Based Spectral Reconstruction for Equivalence Ratio Measurement in Premixed Air-Methane Flames Using RGB Imaging,” *Combustion Science and Technology*, 2024, doi: 10.1080/00102202.2024.2435303.
[20] X. Liu, H. Zhou, Y. Lai, and Y. Zhang, “Equivalence ratio independence and dependence ranges of system responses for a nonlinear thermoacoustic oscillation in a Rijke tube,” *J Sound Vib*, vol. 547, Mar. 2023, doi: 10.1016/j.jsv.2022.117545.
[21] L. Zhou, D. Zeng, D. Li, and M. Chaos, “Total radiative heat loss and radiation distribution of liquid pool fire flames,” *Fire Saf J*, vol. 89, pp. 16–21, Apr. 2017, doi: 10.1016/j.firesaf.2017.02.004.
[22] Y. Lai *et al.*, “Characterisation of wood combustion and emission under varying moisture contents using multiple imaging techniques,” *Fuel*, vol. 373, p. 132397, Oct. 2024, doi: 10.1016/j.fuel.2024.132397.
[23] M. B. Stuart, M. Davies, M. J. Hobbs, T. D. Pering, A. J. S. McGonigle, and J. R. Willmott, “High-Resolution Hyperspectral Imaging Using Low-Cost Components: Application within Environmental Monitoring Scenarios,” *Sensors*, vol. 22, no. 12, Jun. 2022, doi: 10.3390/s22124652.
[24] M. Si, Q. Cheng, Q. Zhang, D. Wang, Z. Luo, and C. Lou, “Study of temperature, apparent spectral emissivity, and soot loading of a single burning coal particle using hyper-spectral imaging technique,” *Combust Flame*, vol. 209, pp. 267–277, Nov. 2019, doi: 10.1016/j.combustflame.2019.08.003.
[25] H. Liu, S. Zheng, H. Zhou, and C. Qi, “Measurement of distributions of temperature and wavelength-dependent emissivity of a laminar diffusion flame using hyper-spectral imaging technique,” *Meas Sci Technol*, vol. 27, no. 2, Dec. 2015, doi: 10.1088/0957-0233/27/2/025201.
[26] Y. Lai *et al.*, “Advanced visualisation of biomass charcoal combustion dynamics using MWIR hyperspectral and LWIR thermal imaging under varied airflow conditions,” *Fuel*, vol. 378, p. 132901, Dec. 2024, doi: 10.1016/j.fuel.2024.132901.

[27] Y. Lai *et al.*, "Investigation of forced flow orientations on the burning behaviours of wooden rods using a synchronised multi-imaging system," *Proceedings of the Combustion Institute*, 2022, doi: 10.1016/j.proci.2022.07.057.
[28] Y. Lai, X. Wang, T. B. O. Rockett, J. R. Willmott, and Y. Zhang, "Investigation into wind effects on fire spread on inclined wooden rods by multi-spectrum and schlieren imaging," *Fire Saf J*, vol. 127, Jan. 2022, doi: 10.1016/j.firesaf.2021.103513.
[29] L. S. Rothman *et al.*, "The HITRAN2012 molecular spectroscopic database," *J Quant Spectrosc Radiat Transf*, vol. 130, pp. 4–50, Nov. 2013, doi: 10.1016/j.jqsrt.2013.07.002.
[30] M. E. Baumgardner and J. Harvey, "Analyzing OH*, CH*, and C2* chemiluminescence of bifurcating FREI propane-air flames in a micro flow reactor," *Combust Flame*, vol. 221, pp. 349–351, Nov. 2020, doi: 10.1016/j.combustflame.2020.08.009.
[31] Y. K. Jeong, C. H. Jeon, and Y. J. Chang, "Evaluation of the equivalence ratio of the reacting mixture using intensity ratio of chemiluminescence in laminar partially premixed CH4-air flames," *Exp Therm Fluid Sci*, vol. 30, no. 7, pp. 663–673, Jul. 2006, doi: 10.1016/j.expthermflusci.2006.01.005.
[32] T. P. Clark, "National Advisory Commitiee Studies of OH, CO, CH and C2 Radiation from Laminar and Turbelent Propane-Air and Ethylene-Air Flames," 1958.
[33] M. E. Tonarely, T. Genova, A. J. Morales, D. Micka, D. Knaus, and K. A. Ahmed, "Four-Line C2*/CH* Optical Sensor for Chemiluminescence Based Imaging of Flame Stoichiometry," *Sensors*, vol. 22, no. 15, Aug. 2022, doi: 10.3390/s22155665.
[34] C. K. Law, *Combustion Physics*. Cambridge University Press, 2006. doi: 10.1017/CBO9780511754517.
[35] O. Park, P. S. Veloo, and F. N. Egolfopoulos, "Flame studies of C2 hydrocarbons," *Proceedings of the Combustion Institute*, vol. 34, no. 1, pp. 711–718, 2013, doi: 10.1016/j.proci.2012.06.159.
[36] R. B. K. Mount and W. Observatory, "Relative transition probabilities of the Swan bands pf Carbon*," 1922.